applied sciences

MDPI

*Article*

# Research on the Dynamics of the Space Tubular Expandable Structure Driving Deployment Unit

**Weiqi Huang [1], Yingjun Guan [1], Hao Wang [1], Huanquan Lu [1] and Huisheng Yang [2,*]**

[1] School of Mechatronic Engineering, Changchun University of Technology, Changchun 130012, China
[2] Changchun Institute of Optics, Fine Mechanics and Physics, Chinese Academy of Sciences, Changchun 130033, China
* Correspondence: ciomp_yhsh@126.com; Tel.: +86-155266825699

**Featured Application: The drive and deployment unit of the variable diameter internal drive device described in this paper is primarily intended for use in space deployment structures. This innovative mechanism is expected to serve as a potential deployment mechanism for large-aperture space telescopes, providing the capability to explore distant deep space.**

**Abstract:** The limitations associated with traditional screw-based and cable-based deployment mechanisms for space deployable structures, such as deployment stiffness, accuracy, and distance, are effectively overcome by introducing the concept of a variable diameter internal drive device. To enhance stability during the discontinuous surface transition phase inside the tubular structure, a thin-walled flexible beam structure is adopted for the driving deployment unit. The analysis employs the spatial absolute nodal coordinate formulation, integrating the pose states of each node into the global coordinate system. The three-dimensional displacement field and rotational angle changes at different time intervals are obtained using the unit shape function matrix and Kirchhoff theory. Subsequently, a dynamic model of the corresponding spatial nodes is established using the virtual work principle. This significant improvement enhances the dynamic characteristics of the coupled rigid-flexible deformation of the driving deployment unit under radial and axial external forces, surpassing the previously used flexible beam structure. The dynamic simulation analysis is performed using the finite element method and validated through experimental tests. The experimental results confirm the driving deployment unit's stability and successful achievement of the desired functionalities, as demonstrated by the endpoint displacement, three-dimensional centroid displacement, and trajectory rotation angle.

**Keywords:** variable diameter internal drive device; flexible beam structure; thin-walled flexible beam structure; absolute nodal coordinate formulation; driving deployment unit



**Citation:** Huang, W.; Guan, Y.; Wang, H.; Lu, H.; Yang, H. Research on the Dynamics of the Space Tubular Expandable Structure Driving Deployment Unit. *Appl. Sci.* **2023**, *13*, 8969. https://doi.org/10.3390/app13158969

Academic Editor: Jérôme Morio

Received: 16 June 2023
Revised: 2 August 2023
Accepted: 3 August 2023
Published: 4 August 2023



## 1. Introduction

According to the 125 most challenging scientific questions published by Science in 2005, 16% of the issues are related to the universe and Earth, with the top question being the composition of the universe. Space telescopes are indispensable tools for human perception and exploration of the universe; however, they are currently limited by launch space and are transitioning from monolithic to modular research. As a result, space deployable structures play a crucial role in modular space telescopes. These telescopes are typically designed to undergo a process from a compact stowed configuration to full deployment through space deployable mechanisms [1–6]. Over the past few decades, various driving techniques have been employed to enhance the deployment capabilities of space deployable mechanisms, including hinged, thin-walled tubular, cylindrical, and wrapped configurations [7–9]. However, the tubular space deployable mechanism exhibits more prominent capabilities in terms of deployment stiffness, strength, and accuracy. Notably, the Telescopic Tube

Mast (TTM) developed by Northrop Grumman for the ISIS (Inflatable Sunshield In Space) system achieved a fully extended length of 6.70 m [10]. Mechanical analysis conducted by Mehran Mobrem et al. on the deployment and retraction of TTM, as shown in Figure 1b, demonstrated that its stiffness and frequencies were better suited for space applications compared to other space deployable mechanisms [11]. Additionally, Fengwei Guan et al. investigated the TTM in the sunshield deployment mechanism of a space telescope and simulated its structural status under axial loads in space, proving that the 8 m long TTM could stably move under a 50 N axial load [12]. However, current fixed-drive devices (screw-nut or cable-driven) used in the TTM result in a short deployment distance and a heavy mass [13–15]. To address this issue, a three-dimensional structure called the variable radial internal drive device (Figure 2) was developed to achieve step-by-step deployment with a smaller mass for the tubular structure while maximizing the extension distance. The effective and stable transition between the non-continuous surfaces at different stages within the tubular structure is currently a critical technical challenge that needs to be addressed to ensure the successful deployment of space telescopes. To overcome this challenge, conducting a flexible multibody dynamics analysis on the non-continuous surfaces during the transitional phase of the variable radial internal drive device is of utmost importance, as it will provide valuable insights into the behavior and reliability of the system.

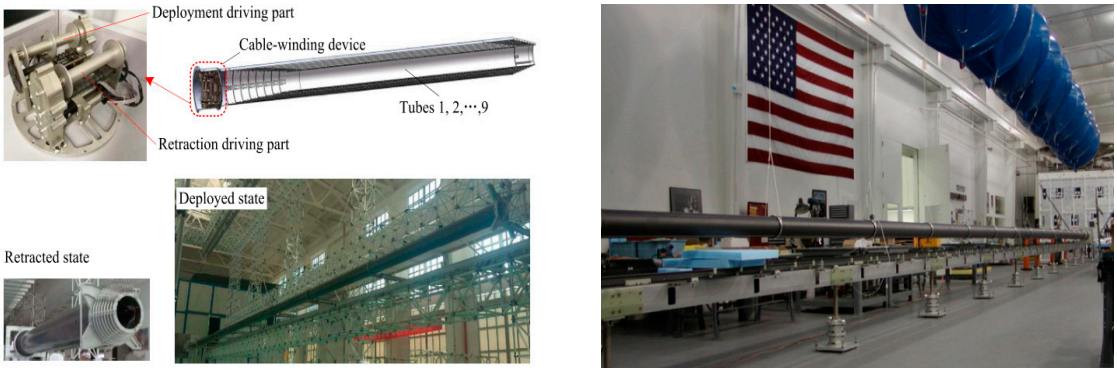


**Figure 1.** (**a**) Tubular (TTM) space deployable mechanism; (**b**) Mechanical testing of the 34.4 m TTM.

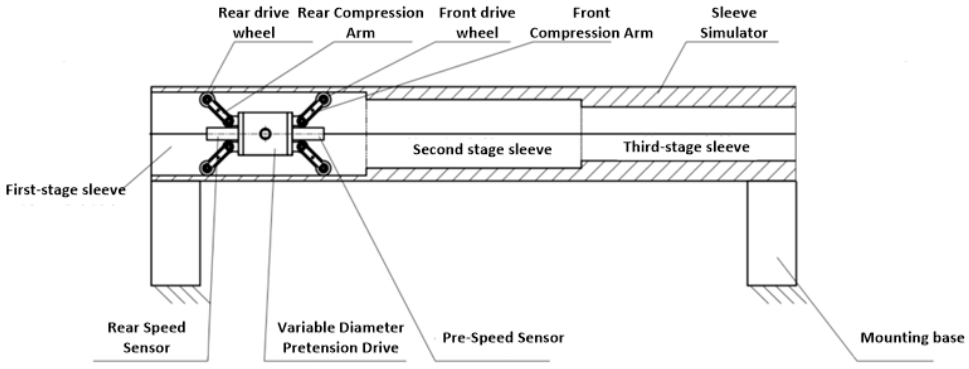


**Figure 2.** Schematic diagram of the variable radial internal drive device in TTM.

In recent years, researchers both domestically and internationally have extensively studied the flexible multibody dynamics analysis of structures with thin-walled characteristics or flexible beam structures, due to their importance in various engineering applications. These structures often exhibit complex deformations and require accurate analysis methods to understand their behavior. The earliest approach used the Kane's Equations of Motion (KED) method [16] to address flexible multibody dynamics. However, this method neglected the

effects of elastic components' motion within their range and gradually revealed limitations in the analysis of coupled fields. To overcome these limitations, the Floating Frame of Reference method (FFR) [17] was proposed, introducing inertial coupling between the motion of rigid components and elastic deformation. However, the nonlinearity of its system matrix significantly impacts the solution of dynamic equations [18,19], leading to reduced accuracy in solving deformation problems. To address these issues, Shabana proposed the absolute nodal coordinate formulation (ANCF) [20,21] based on finite element and continuum mechanics theories. In ANCF, the nodal coordinates of elements are represented by position vectors and slope vectors, instead of the traditional nodal angular coordinates used in finite elements. Additionally, ANCF derives a constant mass matrix, and its system dynamic equations do not include Coriolis and centrifugal force terms, which improves computational efficiency. Therefore, these advantages make the absolute nodal coordinate formulation more suitable for flexible multibody systems compared to other traditional methods.

Zhang Dayu from Northwestern Polytechnical University [22] conducted in-depth research on flexible beam structures using the absolute nodal coordinate formulation (ANCF). The study focused on modeling flexible beams, numerical solutions of the differential-algebraic equations for multibody systems, and applications. The research proposed a novel multibody system modeling method that considers pin joints, effectively addressing the rigid-flexible coupling dynamics problem in spacecraft solar panels and flexible caterpillar tracks with pin joints. Li Boyu [23] aimed to address the numerical simulation issues of slender thin-walled beams with different cross-sectional shapes under large rotations and deformations. Within the framework of the absolute nodal coordinate formulation, a new method was proposed, employing Lagrange interpolation to construct the displacement field of thin-walled beam cross-sections. Lin Shiyang from Harbin Institute of Technology [24] conducted research on dynamic modeling, analysis, and motion control of typical flexible attachments in spacecraft, such as large trusses and robotic arms, based on the absolute nodal coordinate formulation. The study validated the applicability of the absolute nodal coordinate formulation in modeling flexible components, providing valuable insights into the behavior of such structures. Wu Maoqi and colleagues [25] developed a more accurate deformation reconstruction method based on the absolute nodal coordinate formulation, allowing for further extension in the application direction using existing mechanical tools. The method was optimized using a planar beam as an example, and the results demonstrated that the absolute nodal coordinate formulation is beneficial for improving optimization accuracy and efficiency.

Kai Luo and colleagues [26] proposed a new formulation of the absolute nodal coordinate formulation (ANCF) for hyperelastic thin shell finite elements based on the Kirchhoff–Love theory. The study derived the two-dimensional compressible Neo-Hookean constitutive model and the two-dimensional incompressible Mooney–Rivlin constitutive model for ANCF shell elements under plane stress conditions. Additionally, they utilized continuum mechanics to derive efficient analytical formulas for the internal forces and their Jacobians within the shell element, enhancing the understanding and analysis of hyperelastic thin shell structures. Qingjun Li and colleagues [27] presented a unified modeling method for large-scale flexible space structures based on the absolute nodal coordinate formulation. By employing Kronecker products to express various ANCF element shape functions in a unified form, the study derived motion equations through the Hamilton's principle. This approach provides a versatile and systematic approach to modeling large-scale flexible structures, aiding in their design and analysis. Cheng Zhang and colleagues [28] proposed a mechanical analysis model suitable for flexible structures based on the absolute nodal coordinate formulation. By using gradient coordinates instead of traditional angular coordinates in the global coordinate system, they established a mapping relationship between parameters in the current configuration and the reference configuration. This method offers an effective means to analyze the behavior of flexible structures under different loading conditions. Astrid Pechstein and colleagues [29] applied the absolute nodal coordinate formulation to beam structures and derived motion equations for axial motion beams based on

the generalized Lagrange equations in the Lagrange–Euler sense. This research contributes to the understanding of the dynamic behavior of beams and their applications in various engineering systems. Gengxiang Wang [30] treated the dynamic platform of a parallel mechanism as a thin plate element based on the absolute nodal coordinate formulation. By employing the elastic middle surface method, they effectively reduced high-frequency vibration modes, improving the stability and performance of the dynamic platform. The introduction of tangent coordinates to define joint coordinate systems further enhanced the modeling and analysis of flexible-rigid coupled systems. Jingchen Hu and colleagues [31] proposed a recursive algorithm based on the absolute nodal coordinate formulation for dynamic analysis of multi-flexible-body systems with nonlinear large deformations. By describing flexible bodies using ANCF and establishing kinematic and dynamic recursive relationships based on the Articulated Body Algorithm (ABA), the study provides a powerful and efficient method for analyzing complex flexible multibody systems. Yang Dan and colleagues [32] developed a new combined element model based on the absolute nodal coordinate formulation, which derived consistent deformation conditions for two thin plate contact interfaces. This study contributes to the accurate and reliable modeling of contact interactions in thin plate structures, making it valuable for various engineering applications. Fangfang Sheng and colleagues [33] introduced a new model based on the absolute nodal coordinate formulation using the gradient method. By applying this model to nonlinear dynamic analysis of elastic line structures under tension and deformation conditions, the study demonstrated good accuracy and computational efficiency in obtaining results, providing a promising approach for analyzing complex line structures.

Based on extensive research conducted by domestic and international scholars on flexible beam structures or thin-walled flexible beam structures, it has been found that the use of the absolute nodal coordinate formulation (ANCF) offers significant advantages over other flexible multibody dynamic analysis methods in terms of computational accuracy and cost. However, there is limited literature on the application of spatial ANCF for the dynamic analysis of the parallel triangular configuration of thin-walled flexible beam structures, especially in the context of inner-drive unit components of deployable cylindrical structures. To address this gap, this paper first constructs a flexible multibody dynamic analysis model for the inner-drive unit of a deployable cylindrical structure based on the spatial ANCF. This model analyzes the motion states of the driving deployment unit and dynamically models the parallel triangular configuration of the thin-walled flexible beam structure using ANCF. The proposed planar triangular element configuration, with its unique design, aims to enhance the adaptability of the coupled rigid-flexible structure within the deployable cylindrical structure of a space telescope when subjected to radial and axial external forces. By superimposing this coupled rigid-flexible structure in spatial orientation, a parallel configuration is formed, ensuring structural integrity during deployment. To validate the proposed model and assess its performance, finite element analysis is employed to simulate and analyze a virtual prototype. Subsequently, a 1:1 experimental prototype is established to conduct stability tests on the driving deployment unit. This enables the realization of both the driving and stowing functions of the thin-walled flexible beam structure with the triangular configuration within the deployable cylindrical structure while maintaining more stable structural characteristics.

The paper is structured as follows: Section 2 focuses on analyzing the motion states of the space structure. We then proceed with the establishment of displacement fields for both the flexible beam structure and the thin-walled flexible beam structure. Next, we delve into the dynamic equations for the thin-walled flexible beam structure, followed by the dynamic equations for the triangular configuration and the parallel structure system. We also perform trajectory fitting for the axial deployment within the deployable cylindrical structure using node displacement and node velocity calibration. Moving on to Section 3, we employ the finite element analysis method to capture the pose variations of the driving deployment unit at different time points. Additionally, we establish an explicit dynamic coupling field under the pre-tensioned state. Section 4 involves the construction of a test prototype, enabling us to conduct stability tests on the driving deployment unit. Lastly, in

Section 5, we provide a comprehensive summary of the entire paper and offer insights into the scope of future work.

## 2. Methods

### *2.1. Motion Analysis of the Driving Deployment Unit*

The inner-drive unit within the deployable cylindrical structure of a space telescope plays a critical role in achieving both axial deployment and radial pre-tensioning capabilities for motion deployment and stowing functions. This deployable cylindrical structure is an essential part of a space telescope, enabling its optical components to be precisely positioned at designated locations. Figure 3 illustrates the driving deployment unit, which is distributed within the inner-drive unit. This unit is responsible for driving the axial deployment of the inner-drive unit inside the cylindrical structure, sequentially expanding each level of the cylindrical tube to facilitate the positioning of optical components at the end of the third-level cylindrical tube.

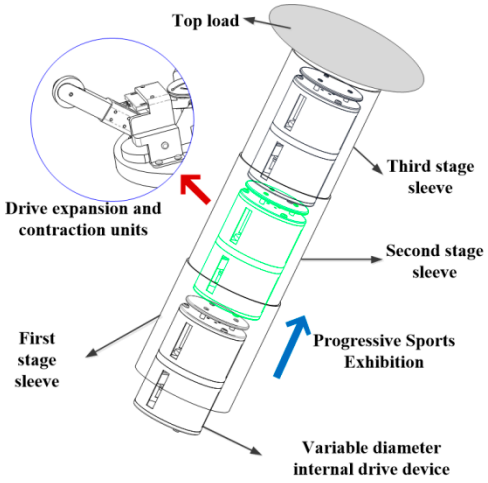


**Figure 3.** Motion states within the cylindrical structure.

In Figure 4, we present a simplified model of the driving deployment unit in the XOY coordinate system. Point A denotes the rotation point, while Point B serves as the pre-tensioning point providing radial pre-tensioning load. Point C represents the connection point between the driving arm component and the pre-tensioning component, and finally, Point D is the contact point between the driving deployment unit and the inner wall of the cylindrical structure.

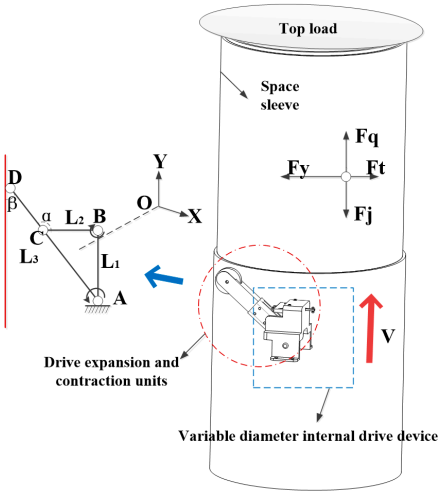


**Figure 4.** The triangular configuration of the unit.

When the driving and retracting unit is working inside the sleeve, the driving force provides traction $F_q$; the pre tightening component provides the radial pre tightening force $F_y$; the reaction force $F_t$ is formed on the inner wall of the sleeve; a reverse friction force $F_j$ is formed between the traction force $F_q$ and the inner wall of the sleeve; when working, it is subject to the gravity of the earth G. According to the force analysis when driving the retracting unit, with the decrease of sleeve diameter, point A rotates clockwise, and the included angle β reduce. If the length of $L_1$ between two points AB is unchanged, the included angle $\alpha$ will also decrease. If the included angle is maintained $\alpha$, the length of $L_2$ needs to be adjusted. In order to maintain a stable triangular configuration ABC, $L_1$, $L_2$, and $L_3$ are set as variable beam elements to cope with the force changes caused by the change of sleeve diameter and maintain the stability of the driving retraction process.

### *2.2. The Spatial Nodal Dynamic Description of the Thin-Walled Flexible Beam Structure*

To achieve both driving and pre-tensioning functions, the inner-drive unit must withstand significant axial forces and bear strong bending moments. Therefore, we have opted to replace each rod element with beam elements, utilizing a triangular element structure. By maintaining the coupled rigid-flexible state of the inner-drive unit and considering the thin-walled characteristics of internal components, we conduct analyses on each flexible beam structure using a thin-walled configuration.

To achieve smooth inter-stage transitions within the inner-drive unit of the deployable cylindrical structure of a space telescope and effectively suppress nonlinear vibrations among internal components, conducting motion-elastic dynamic analysis of the triangular configuration of the thin-walled flexible beam structure is of utmost importance. As discussed in Section 1, the absolute nodal coordinate formulation (ANCF) is based on finite element and continuum mechanics theories, providing a more accurate description of structural self-rotation and deformation under external forces. To provide a clearer explanation of the dynamic analysis of the thin-walled flexible beam structure using the absolute nodal coordinate formulation (ANCF), we establish a unit nodal matrix based on the flexible beam structure and then discretize the matrix. Furthermore, we extract the position vectors of the mid-surface, forming a collection of position vectors for any point on the mid-surface of the thin-walled flexible beam structure. By utilizing the strain and curvature of the unit, we transform the unit mass matrix to obtain the unit dynamic equations. Moreover, we obtain the generalized external forces using the principle of virtual work and introduce them into structures with different configurations and morphologies. During this process, we transform the unit mass matrix of the thin-walled flexible beam element to derive the corresponding unit mass matrix. Finally, by constructing the dynamic equations, we can obtain node velocities and node displacements. The specific process is illustrated in Figure 5.

#### 2.2.1. Analysis of the Displacement Field in the Flexible Beam Structure

The global position vector r of any point on the space absolute coordinate flexible beam element can be described by the global shape function [34,35] and the absolute node coordinates of the element as follows:

$$\mathbf{r} = \mathbf{S}(x, y, z)\mathbf{e} \tag{1}$$

where: $\mathbf{S}$ is the element shape function matrix; $x, y, z$ are the position coordinates of nodes in the global coordinate system; $\mathbf{e}$ is the absolute node coordinate vector, which is represented by the node displacement vector and slope vector. Figure 6 shows the change of the global position vector r.

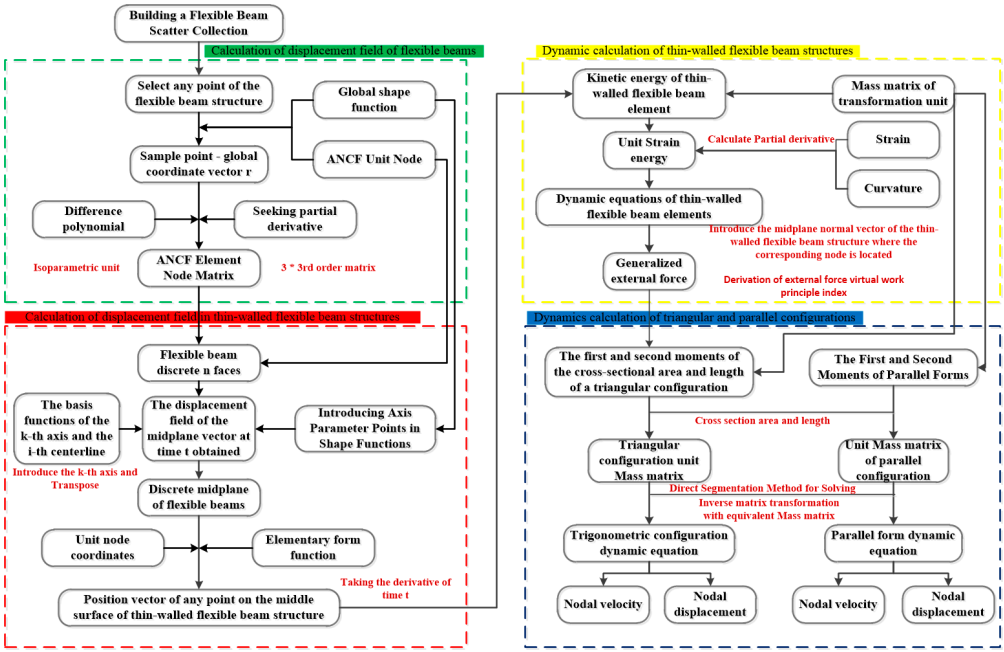


**Figure 5.** Space nodal dynamic description flowchart.

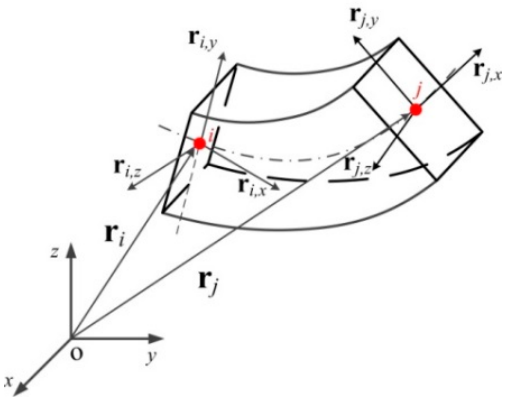


**Figure 6.** The ANCF (absolute nodal coordinate formulation) coordinate vector.

Difference polynomial of displacement field of this element:

$$\mathbf{r} = \begin{bmatrix} r_1 \\ r_2 \\ r_3 \end{bmatrix} = \begin{bmatrix} a_0 + a_1 x + a_2 y + a_3 z + a_4 xy + a_5 xz + a_6 x^2 + a_7 x^3 \\ b_0 + b_1 x + b_2 y + b_3 z + b_4 xy + b_5 xz + b_6 x^2 + b_7 x^3 \\ c_0 + c_1 x + c_2 y + c_3 z + c_4 xy + c_5 xz + c_6 x^2 + c_7 x^3 \end{bmatrix} \tag{2}$$

The displacement vector and gradient vector in node coordinates can be obtained through rigid body motion from the undeformed reference configuration. The three-dimensional beam element with absolute node coordinates is an isoparametric element [36,37]. Each element consists of 2 nodes, and each node has 12 node coordinates. When the beam element is undeformed, its length is denoted by "l". The absolute node coordinate vector of the element can be expressed as follows:

$$\mathbf{e} = \left[\mathbf{r}_i \ \mathbf{r}_{i,x} \ \mathbf{r}_{i,y} \ \mathbf{r}_{i,z} \ \mathbf{r}_j \ \mathbf{r}_{j,x} \ \mathbf{r}_{j,y} \ \mathbf{r}_{j,z}\right]^{\mathrm{T}} \tag{3}$$

where: $\mathbf{r}_i$ and $\mathbf{r}_j$ are the absolute position vectors of node k on unit j; $\mathbf{r}_{,x}$, $\mathbf{r}_{,y}$, and $\mathbf{r}_{,z}$ are the partial derivative vectors of element nodes $i$ and $j$ in the $x$, $y$, and $z$ directions, respectively, which are used to describe the deformation of the beam cross-section in this direction.

$\mathbf{r}_{,x} = \partial\mathbf{r}/\partial x, \mathbf{r}_{,y} = \partial\mathbf{r}/\partial y. \mathbf{r}_{,z} = \partial\mathbf{r}/\partial z$. Thus, the overall node coordinate vector of the element can be written as:

$$e = \left[ r_{i1}, r_{i2}, r_{i3}, \frac{\partial r_{i1}}{\partial x}, \frac{\partial r_{i2}}{\partial x}, \frac{\partial r_{i3}}{\partial x}, \frac{\partial r_{i1}}{\partial y}, \frac{\partial r_{i2}}{\partial y}, \frac{\partial r_{i3}}{\partial y}, \frac{\partial r_{i1}}{\partial z}, \frac{\partial r_{i2}}{\partial z}, \frac{\partial r_{i3}}{\partial z} \right. \\ \left. r_{j1}, r_{j2}, r_{j3}, \frac{\partial r_{j1}}{\partial x}, \frac{\partial r_{j2}}{\partial x}, \frac{\partial r_{j3}}{\partial x}, \frac{\partial r_{j1}}{\partial y}, \frac{\partial r_{j2}}{\partial y}, \frac{\partial r_{j3}}{\partial y}, \frac{\partial r_{j1}}{\partial z}, \frac{\partial r_{j2}}{\partial z}, \frac{\partial r_{j3}}{\partial z} \right] \tag{4}$$

It can be observed that each beam element has 24 node coordinates, which is also a disadvantage of the absolute node coordinates method. The large number of node coordinates results in reduced calculation efficiency.

The element shape function matrix can be defined using the element interpolation polynomial and node coordinates:

$$\mathbf{S} = \left[ S_1 I \; S_2 I \; S_3 I \; S_4 I \; S_5 I \; S_6 I \; S_7 I \; S_8 I \right] \tag{5}$$

where matrix I is a $3 \times 3$ order identity matrix:

$$\begin{aligned} &S_1 = 1 - 3\xi^2 + 2\xi^3, S_2 = l(\xi - 2\xi^2 + \xi^3) \\ &S_3 = l(\eta - \xi\eta), S_4 = l(\zeta - \xi\zeta) \\ &S_5 = 3\xi^2 - 2\xi^3, S_6 = l(-\xi^2 + \xi^3) \\ &S_7 = l\xi\eta, S_8 = l\xi\zeta) \end{aligned} \tag{6}$$

Including: $\xi$, $\eta$, and $\zeta$ are dimensionless parameter; $\xi = x/l, \eta = y/l, \zeta = z/l$, $l$ is the length of the beam element in the undeformed configuration.

2.2.2. Analysis of the Displacement Field in the Thin-Walled Flexible Beam Structure

Building upon the flexible beam structure, we conduct a displacement field analysis for the flexible beam with thin-walled characteristics. The primary objective is to achieve both driving transmission and pre-tensioning transmission while maintaining lightweight characteristics. In contrast to the displacement field analysis of the flexible beam structure in the previous Section 2.2.1, this section employs the middle surface characteristics to more accurately describe the displacement field variation of the flexible beam structure with thin-walled characteristics. To better illustrate the concept, Figure 7 illustrates a schematic diagram of the thin-walled flexible beam structure.

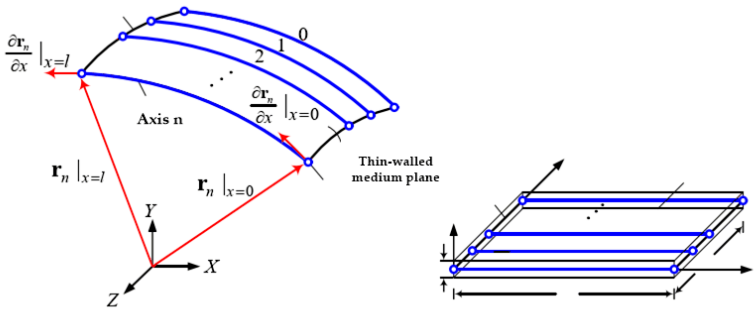


**Figure 7.** Schematic diagram of thin-walled flexible beam element.

As shown in Figure 4, since the wall thickness $h$ of the thin-walled flexible beam element is much smaller than the section width $w$, according to Kirchhoff's thin plate theory, the displacement field of the thin-walled flexible beam element can be determined from its midplane. In the global coordinate system, the displacement field of the position vector $r$ of any point on the middle plane of the thin-walled flexible beam element at time $t$ is given by the following Equation (7):

$$\mathbf{r}(x, y, t) = \sum_{k=0}^{n} \mathbf{r}_k(x, t) L_{k,n}(y) \tag{7}$$

where: $\mathbf{r}_k$ is the $k$-th axis of the middle plane. The $k$-th axis in the thin-walled beam element can be expressed by the absolute node coordinate method under three-dimensional coordinates as follows:

$$\mathbf{r}_k(x,t) = \mathbf{S}(x)\mathbf{e}_k(t) \tag{8}$$

where: $\mathbf{r}_k(x,t)$ is the function of the parameter $x$ and time $t$ in the local coordinates, where $\mathbf{S}(x)$ is still the shape function matrix, and $\mathbf{e}_k(t)$ is the value of the node coordinate matrix of the $k$-th axis at time $t$. Where $\mathbf{e}_k(t)$ is:

$$\mathbf{e}_k = \left[ \left.\mathbf{r}_k^{\mathrm{T}}\right|_{x=0} \left.\frac{\partial \mathbf{r}_k^{\mathrm{T}}}{\partial x}\right|_{x=0} \left.\mathbf{r}_k^{\mathrm{T}}\right|_{x=l} \left.\frac{\partial \mathbf{r}_k^{\mathrm{T}}}{\partial x}\right|_{x=l} \right]^{\mathrm{T}} \tag{9}$$

In the formula, $T$ is the transposition and $l$ is the length of the thin-walled flexible beam element. In Formula (7), the basis function $L_{k,n}$ defines the corresponding centerline on the middle plane of the thin-walled flexible beam element, which is a function of the local coordinate parameter $y$. The interpolation form of basis function $L_{k,n}$ is:

$$L_{k,n} = \prod_{\substack{i=0 \\ i\neq k}}^{n} \frac{(y-y_i)}{(y_k-y_i)} \tag{10}$$

where: $y_i$ is the node coordinate of the $i$-th axis. Through the above displacement field of thin-walled flexible beam element, for different $n$-order Lagrangian interpolation, there is corresponding thin-walled flexible beam element model $L_n$, and the coordinate $q$ of the element node is:

$$\mathbf{q} = \left[\mathbf{e}_0^{\mathrm{T}}\ \mathbf{e}_1^{\mathrm{T}}\ \cdots\ \mathbf{e}_n^{\mathrm{T}}\right] \tag{11}$$

The unit shape function is:

$$\mathbf{N}(x,y) = \left[L_{0,n}(y)S(x)L_{1,n}(y)S(x)\ \cdots\ L_{n,n}(y)S(x)\right] \tag{12}$$

Through Equations (11) and (12), the position vector of any point on the middle plane of the thin-walled flexible beam element is:

$$\mathbf{r}(x,y,t) = \mathbf{N}(x,y)\mathbf{q}(t) \tag{13}$$

2.2.3. The Dynamic Equations of the Thin-Walled Flexible Beam Structure

First, derivative of time t of Equation (13) can be used to obtain the element kinetic energy expression of thin-walled flexible beam element:

$$T = \frac{1}{2}\rho h \int_0^w \int_0^l q^T q dx dy = \frac{1}{2} q^T M q \tag{14}$$

where: $\rho$ is the mass density, $h$ is the thickness, $q$ is the coordinates of element nodes, $\mathbf{M}$ is the element mass matrix, and the element mass matrix is:

$$\mathbf{M}\& = \int_V \rho \mathbf{S}^{\mathrm{T}} \cdot \mathbf{S} dV$$

$$\begin{bmatrix}
\frac{13}{35}m\mathbf{I} & \frac{11}{210}lm\mathbf{I} & \frac{7}{20}\rho lQ_z\mathbf{I} & \frac{7}{20}\rho lQ_y\mathbf{I} & \frac{9}{70}m\mathbf{I} & -\frac{13}{420}lm\mathbf{I} & \frac{3}{20}\rho lQ_z\mathbf{I} & \frac{3}{20}\rho lQ_y\mathbf{I} \\
 & \frac{1}{105}l^2m\mathbf{I} & \frac{1}{20}\rho l^2Q_z\mathbf{I} & \frac{1}{20}\rho l^2Q_y\mathbf{I} & \frac{13}{420}lm\mathbf{I} & -\frac{1}{140}l^2m\mathbf{I} & \frac{1}{30}\rho l^2Q_z\mathbf{I} & \frac{1}{30}\rho l^2Q_y\mathbf{I} \\
 & & \frac{1}{3}\rho lI_{zz}\mathbf{I} & \frac{1}{3}\rho lI_{yz}\mathbf{I} & \frac{3}{20}\rho lQ_z\mathbf{I} & -\frac{1}{30}\rho l^2Q_z\mathbf{I} & \frac{1}{6}\rho lI_{zz}\mathbf{I} & \frac{1}{6}\rho lI_{yz}\mathbf{I} \\
 & & \frac{1}{3}\rho lI_{yy}\mathbf{I} & \frac{3}{20}\rho lQ_y\mathbf{I} & \frac{1}{30}\rho l^2Q_y\mathbf{I} & \frac{1}{6}\rho lI_{yz}\mathbf{I} & \frac{1}{6}\rho lI_{yy}\mathbf{I} & \\
 & & & \frac{13}{35}m\mathbf{I} & -\frac{11}{210}lm\mathbf{I} & \frac{7}{20}\rho lQ_z\mathbf{I} & \frac{7}{20}\rho lQ_y\mathbf{I} & \\
 & & & \frac{1}{105}l^2m\mathbf{I} & -\frac{1}{20}\rho l^2Q_z\mathbf{I} & -\frac{1}{20}\rho l^2Q_y\mathbf{I} & & \\
 & & & & \frac{1}{3}\rho lI_{zz}\mathbf{I} & \frac{1}{3}\rho I_{yz}\mathbf{I} & & \\
 & & & & \frac{1}{3}\rho I_{yy}\mathbf{I} & & &
\end{bmatrix} \tag{15}$$

Strain energy of thin-walled flexible beam element:

$$U = U^{\varepsilon} + U^{\kappa} \tag{16}$$

where, $U^{\varepsilon}$ is the membrane strain energy caused by the tension, compression, and other deformation of the middle surface of the thin-walled beam element [38], and $U^{\kappa}$ is the bending strain energy caused by the bending and torsional deformation of the thin-walled beam element. They are:

$$U^{e} = \frac{Eh}{2(1-v^2)} \int_0^w \int_0^1 \varepsilon_x^2 + \varepsilon_y^2 + 2v\varepsilon_x\varepsilon_y + \frac{1}{2}(1-v)\gamma_{xy}^2 \mathrm{d}x\mathrm{d}y \tag{17}$$

$$U^{\kappa} = \frac{Eh^3}{24(1-v^2)} \int_0^w \int_0^l \kappa_x^2 + \kappa_y^2 + 2v\kappa_x\kappa_y + 2(1-v)\kappa_{xy}^2 \mathrm{d}x\mathrm{d}y \tag{18}$$

where, $E$ is Young's modulus and $v$ is Poisson's ratio. The strain and curvature are:

$$\varepsilon_x = \frac{1}{2}\left(\mathbf{r}_x^{\mathrm{T}}\mathbf{r}_x - 1\right), \varepsilon_y = \frac{1}{2}\left(\mathbf{r}_y^{\mathrm{T}}\mathbf{r}_y - 1\right), \gamma_{xy} = \mathbf{r}_x^{\mathrm{T}}\mathbf{r}_y \tag{19}$$

$$\kappa_x = \frac{\mathbf{r}_{xx}^{\mathrm{T}}\mathbf{n}}{\| \mathbf{n} \|^3}, \kappa_y = \frac{\mathbf{r}_{yy}^{\mathrm{T}}\mathbf{n}}{\| \mathbf{n} \|^3}, \kappa_{xy} = \frac{\mathbf{r}_{xy}^{\mathrm{T}}\mathbf{n}}{\| \mathbf{n} \|^3} \tag{20}$$

where: $\mathbf{r}$ is the partial derivative of $x$ or $y$, and $\mathbf{n} = \mathbf{r}_x \times \mathbf{r}_y$ is the normal vector of the mid plane of the thin-walled flexible beam element.

Further obtaining the dynamic equations of the thin-walled flexible beam structure, we can derive them using the Lagrangian equation [39,40] as shown in Formula (21).

$$\frac{\mathrm{d}}{\mathrm{d}t}\left(\frac{\partial T}{\partial \dot{\mathbf{q}}}\right) - \frac{\partial T}{\partial \mathbf{q}} + \frac{\partial U}{\partial \mathbf{q}} = \mathrm{F} \tag{21}$$

where: $T$ is the kinetic energy, $U$ is the strain energy, and $F$ is the generalized external force derived from the virtual work of the external force [41,42].

2.2.4. The Dynamic Equations of the Triangular Configuration

Through the dynamic derivation of the thin-walled flexible beam element in the previous section, to solve the dynamic equation of the triangular configuration of thin-walled flexible beam element combination, first, suppose that each cross section area is $A_1$, $A_2$, $A_3$, each length is $l_1$, $l_2$, $l_3$, and the material is the same material, so the density is $\rho$, I is the order $3 \times 3$ unit matrix, and the first and second moments of the cross section are, respectively:

$$\begin{cases} Q_{y1} = \int\limits_{A1} z dA_1,\ Q_{y2} = \int\limits_{A2} z dA_2,\ Q_{y3} = \int\limits_{A3} z dA_3 \\ Q_{z1} = \int\limits_{A1} y dA_1,\ Q_{z2} = \int\limits_{A2} y dA_2,\ Q_{z3} = \int\limits_{A3} y dA_3 \\ I_{yy1} = \int\limits_{A1} z^2 dA_1,\ I_{yy2} = \int\limits_{A2} z^2 dA_2,\ I_{yy3} = \int\limits_{A3} z^2 dA_3 \\ I_{zz1} = \int\limits_{A1} y^2 dA_1,\ I_{zz2} = \int\limits_{A2} y^2 dA_2,\ I_{zz3} = \int\limits_{A3} y^2 dA_3 \\ I_{yz1} = \int\limits_{A1} yz dA_1,\ I_{yz2} = \int\limits_{A2} yz dA_2,\ I_{yz3} = \int\limits_{A3} yz dA_3 \end{cases} \tag{22}$$

Substitute the parameters in Equation (22) into Equation (15), where $l$ is replaced by $l_1$, $l_2$, $l_3$, and the kinetic energy and strain energy of the system are obtained through Equations (14) and (16). The system dynamics equation can be established by using the traditional finite element assembly method. For the unit mass matrix obtained by substituting

Equation (22) into Equation (15), use the direct integration method to solve the dynamic equation [43], as follows:

$$\mathbf{M}_v\ddot{q}_t = \mathbf{Q} - \mathbf{K}_\mathrm{A}\mathbf{B}_{t-\Delta t} \tag{23}$$

where, $\mathbf{M}_v$ is the equivalent mass matrix,$\mathbf{Q} = \mathbf{Q}_\mathrm{FA} + \mathbf{Q}_\mathrm{gA}$

$$\mathbf{M}_v = \mathbf{M}_\mathrm{A} + \frac{\Delta t^2}{6}\mathbf{K}_\mathrm{A} \tag{24}$$

$$\mathbf{B}_{t-\Delta t} = q_{t-\Delta t} + \Delta t\dot{q}_{t-\Delta t} + \frac{\Delta t^2}{3}\ddot{q}_{t-\Delta t} \tag{25}$$

Then, multiply the left and right ends of Equation (23) by the inverse matrix $\mathbf{M}_v^{-1}$ of the equivalent mass matrix to get.

$$\ddot{q}_t = \mathbf{M}_v^{-1}(\mathbf{Q}_t - \mathbf{K}\mathbf{B}_{t-\Delta t}) \tag{26}$$

After obtaining node acceleration $\ddot{q}_t$ at time $t$, node velocity and node displacement can be calculated by the following formula:

$$\dot{q}_t = \dot{q}_{t-\Delta t} + \frac{\Delta t}{2}\ddot{q}_{t-\Delta t} + \frac{\Delta t}{2}\ddot{q}_t \tag{27}$$

$$q_t = q_{t-\Delta t} + \Delta t\dot{q}_{t-\Delta t} + \frac{\Delta t^2}{2}\ddot{q}_{t-\Delta t} + \frac{\Delta t^2}{6}\ddot{q}_t \tag{28}$$

### *2.3. The Dynamic Fitting of the Parallel Configuration*

To effectively enhance stability, we arrange the thin-walled flexible beam structures in parallel within the spatial telescope tube, forming a parallel configuration and constituting the variable-radius internal driving device, as illustrated in Figure 8.

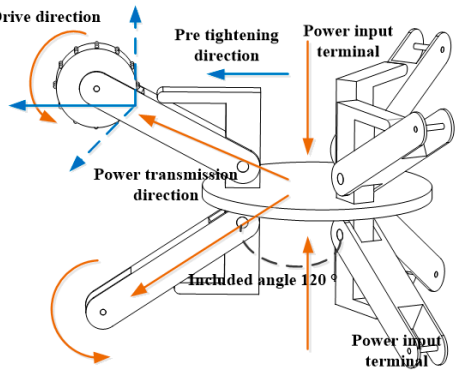


**Figure 8.** Schematic diagram of the parallel symmetrical structure.

To achieve the sequential expansion and driving functions of each level of the spatial telescope tube, we employ a dual-layer symmetrical structure with an angle of 120°. This is accomplished using six identical thin-walled flexible beam triangular unit configurations, as shown in Figure 9, which represents the overall model of the thin-walled flexible beam triangular units. Additionally, from Figure 8, it can be observed that the upper and lower layers of the structure consist of thin-walled flexible beam triangular units on the same side, forming a new triangular configuration that constitutes one-third of the overall variable-radius internal driving device structure. As the variable-radius internal driving device is axially symmetrical, we take a partial structure as an example to derive the kinematics of the parallel configuration of the driving expansion units.

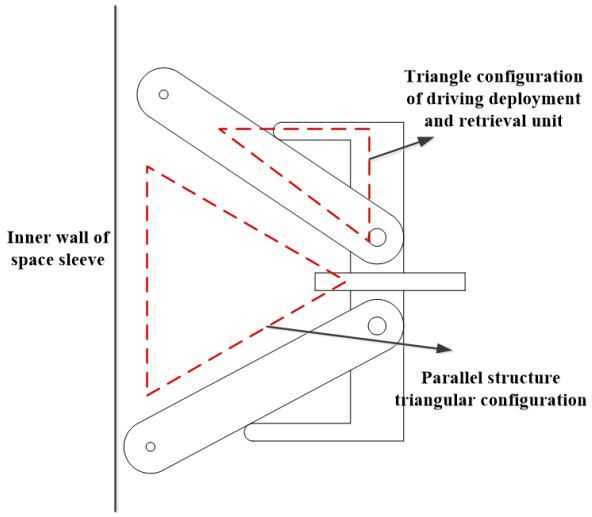


**Figure 9.** Overall configuration of the triangular element.

Taking the dynamic equation in Section 2.2 as an example, the new triangular configuration is further deduced. The section of the longest thin-walled flexible beam element with the same triangular configuration of the upper and lower thin-walled flexible beams is set as $A_4$ and $A_5$. The length is $l_4$ and $l_5$, and the material density is $\rho$, which are respectively substituted into Formula (22) to form:

$$\begin{cases} Q_{y4} = \int\limits_{A4} z dA_4,\ Q_{y5} = \int\limits_{A5} z dA_5 \\ Q_{z4} = \int\limits_{A4} y dA_4,\ Q_{z5} = \int\limits_{A5} y dA_5 \\ I_{yy4} = \int\limits_{A4} z^2 dA_4,\ I_{yy5} = \int\limits_{A5} z^2 dA_5 \\ I_{zz4} = \int\limits_{A4} y^2 dA_4,\ I_{zz5} = \int\limits_{A5} y^2 dA_5 \\ I_{yz4} = \int\limits_{A4} yz dA_4,\ I_{yz5} = \int\limits_{A5} yz dA_5 \end{cases} \tag{29}$$

After substituting Equation (29) into Equation (15) and obtaining the unit mass matrix, we employ the direct integration method for dynamic analysis. First, we obtain the nodal accelerations, and then, utilizing Equations (27) and (28), we determine the nodal velocities and displacements of the new triangular configuration. Figures 10 and 11 illustrate the displacement variations of the driving expansion unit in the parallel structure. We observe that the displacement variations are more uncertain at the free end compared to the constrained end. This uncertainty arises from the thin-walled flexible beam structure's behavior, which exhibits "free end" conditions when not subjected to radial loads but acts as "constrained end" conditions on the discontinuous surface when under radial loads. These conditions are not independent but occur as part of a complete process, where the "free end" temporarily appears due to the unique nature of the internally driven unit with a variable diameter moving within the spatial sleeve involving a transitional discontinuous surface (step-like). Consequently, there is a possibility of momentary failure due to axial friction and radial preloading. Although the occurrence of such a situation is low in probability, considering the overall stability and reliability of the structure [44], its uncertainty is greater than that of the "constrained end" conditions. Therefore, our analysis focuses on the displacement components under the "free end" condition.

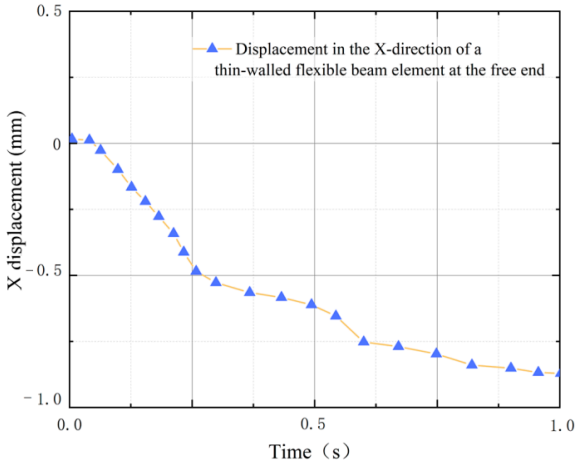


**Figure 10.** The *X*-axis displacement component at the free end node.

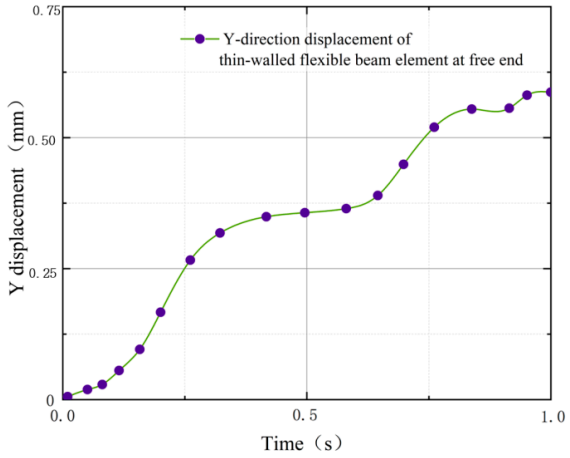


**Figure 11.** The *Y*-axis displacement component at the free end node.

Figure 10 shows that the displacement in the X-direction of the local coordinate system increases negatively with axial expansion, while the radial distance increases positively. Additionally, Figure 11 demonstrates that the displacement in the Y-direction gradually increases over time, exhibiting positive growth in the axial distance. These changes in displacements in the X and Y directions are caused by the reduction in tube diameter. Figure 12 illustrates the midpoint deflection of the thin-walled flexible beam structure in its free-end state.

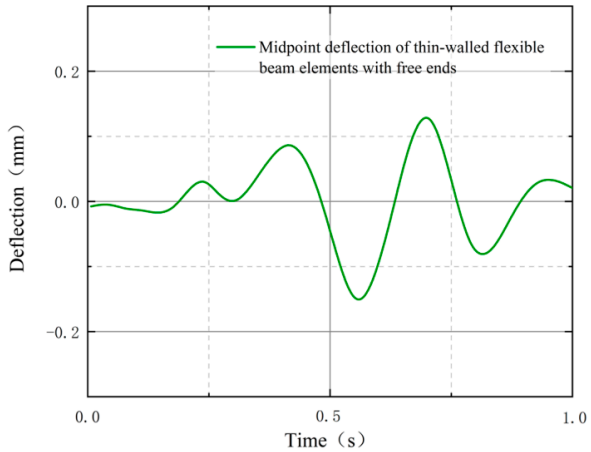


**Figure 12.** The mid-span deflection of the free end state.

Figure 12 shows that as the driving expansion unit transitions among the different stages of the tube, the displacement of the endpoints causes changes in the midpoint deflection at various locations. This observation indicates that during this motion process, the thin-walled flexible beam structure in its free-end state undergoes both tensile and bending deformations. Additionally, Figure 13 illustrates the changes in the displacement field of the thin-walled flexible beam structure in its free-end state.

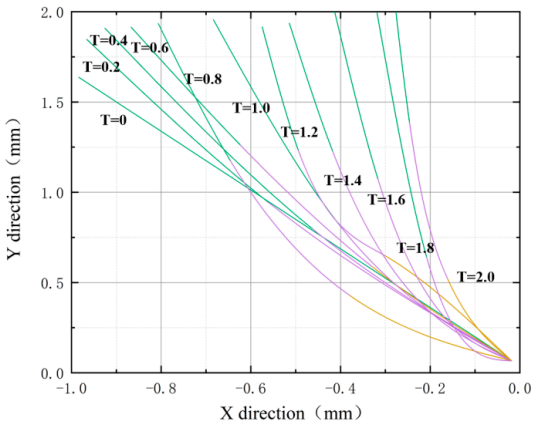


**Figure 13.** The displacement field state at the free end.

It can be found from Figure 13 that when the time interval is 0.2, the change of $L_3$ changes from the initial state T = 0 to the time of T = 2.0 after realizing the function of driving and retracting, the thin-walled flexible beam element produces tension and deformation, resulting in the change of displacement in X and Y directions. Based on the free end, through the analysis of the motion state of the driving expansion unit in the space sleeve, combined with the free end and the constraint end, a complete working state is formed.

Figure 14 illustrates the positional variations of the driving expansion unit at different time intervals in its complete state. At the four time intervals (0.25 s, 0.5 s, 0.75 s, and 1.0 s), the displacement in the X direction of the thin-walled flexible beam structure shows more noticeable changes compared to the displacement of the flexible beam structure from its initial position, while maintaining the same Y height. Similarly, when the X position remains constant, the displacement in the Y direction also undergoes significant changes, which align more closely with the structural characteristics of the thin-walled flexible beam structure.

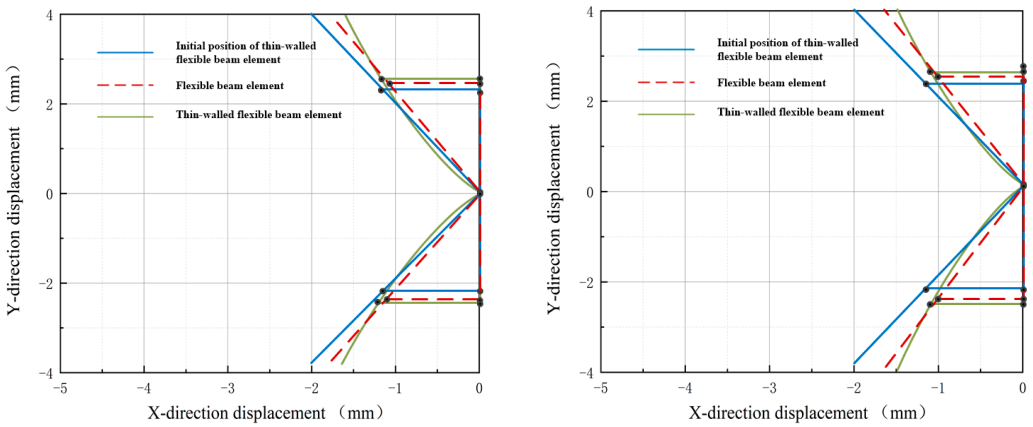


**Figure 14.** *Cont.*

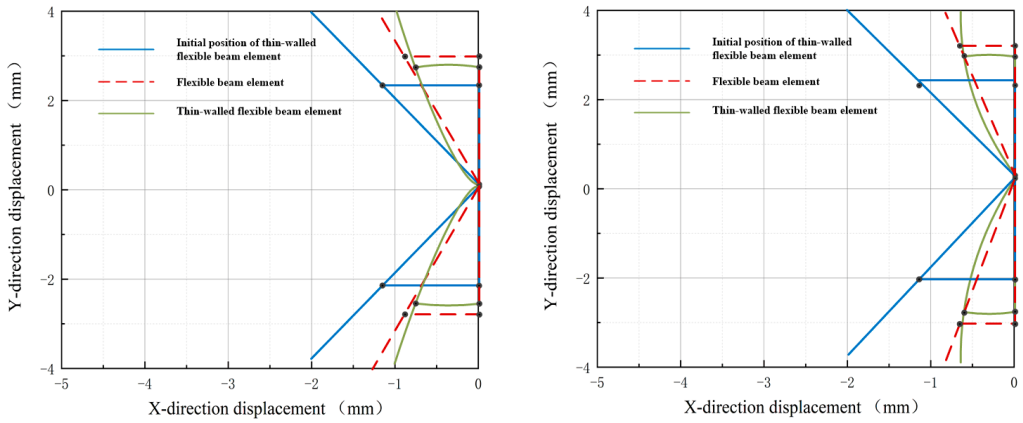


**Figure 14.** Pose variations of the driving deployment unit. (**a**) At the time of 0.25 s; (**b**) At the time of 0.50 s; (**c**) At the time of 0.75 s; (**d**) At the time of 1.00 s.

Figure 15 illustrates the trajectory variations of the axial expansion within the interior of the tube when the driving expansion unit is in an integrated state, considering both constrained and unconstrained conditions. The displacement analysis of the overall parallel structure utilizes a combination of constrained and unconstrained states (free end) as boundary conditions to better approximate the actual operating state and validate the motion trajectory.

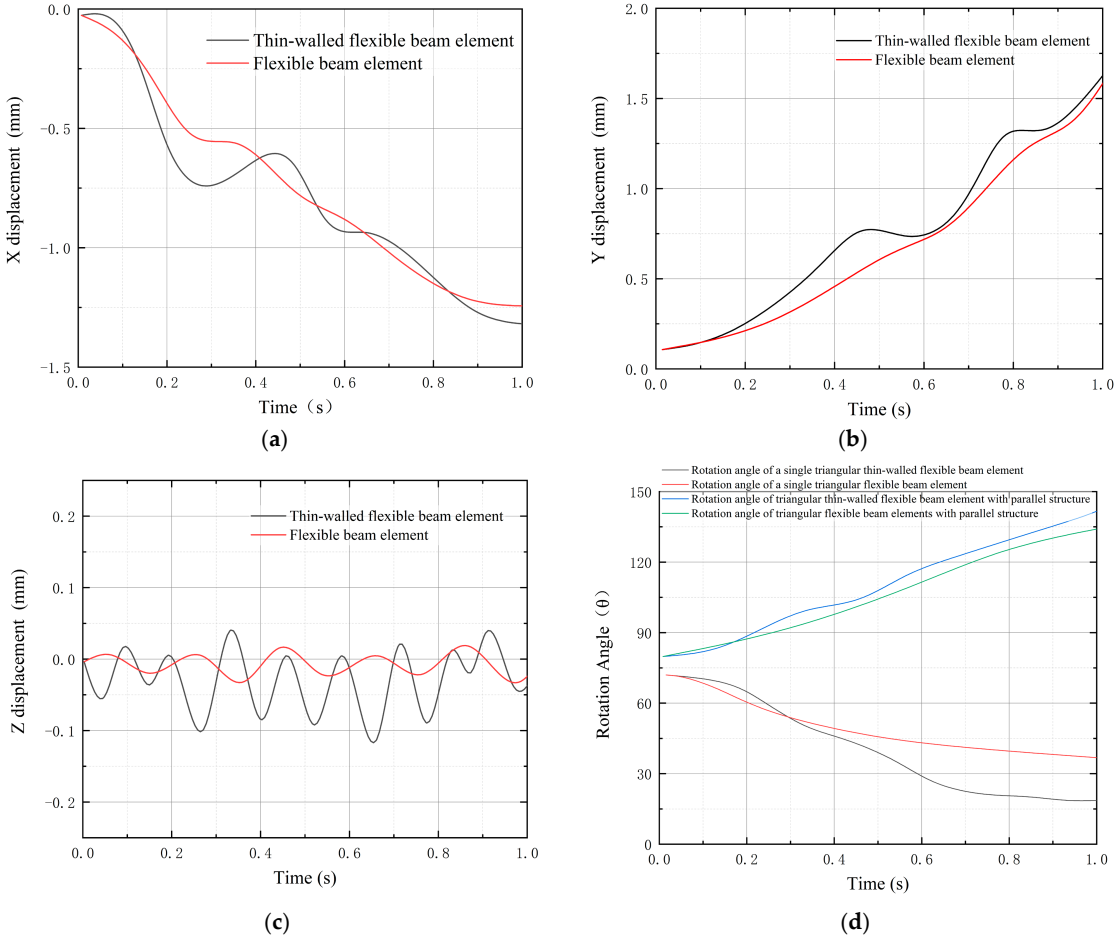


**Figure 15.** Motion trajectory of the driving deployment unit. (**a**) Centroid displacement in the X-direction; (**b**) Centroid displacement in the Y-direction; (**c**) Centroid displacement in the Z-direction; (**d**) Trajectory rotation angle.

Figure 15a,b illustrates the nodal displacements of the flexible beam structure and the thin-walled flexible beam structure using the absolute nodal coordinate formulation (ANCF) method. Within the time interval of 0 to 0.1 s, the displacement variations of their centroids in the x and y directions are not significant. This lack of significant displacement is attributed to the initial motion occurring on the inner surface of the first-level tube. As the diameter of the tube changes, the displacement gradually increases. However, the presence of inter-level discontinuous surfaces at the connections between the various levels of tubes results in observed peaks and valleys during this period.

Figure 15c shows that the thin-walled flexible beam structure exhibits oscillations in the Z direction compared to the flexible beam structure. This is due to its enhanced flexibility and the effect of its own weight. On the other hand, Figure 15d illustrates the angle variations of both the individual and parallel triangle configurations, which consist of the flexible beam structure and the thin-walled flexible beam structure. It is evident from the graph that the angle variations of the individual and parallel triangle configurations with the thin-walled flexible beam structure are more pronounced than those with the flexible beam structure. In conclusion, the driving and unfolding unit constructed with the thin-walled flexible beam structure, as described by the ANCF nodal displacement, better aligns with its operational state within the telescope's sleeve-type deployable structure.

## 3. Finite Element Analysis

### *3.1. Boundary Conditions*

The first step involves modeling the variable-radius inner-drive unit using SolidWorks. Figure 16 presents the complete geometric model of the variable-radius inner-drive unit, with the right side representing the unit in its fully expanded state, and the left side depicting the initial stage of axial deployment of the variable-radius inner-drive unit inside the cylindrical structure. From the figure, it can be observed that the variable-radius inner-drive unit consists of three groups of axially symmetrical driving and stowing units, divided into upper and lower layers. During the axial deployment inside the cylindrical structure, the angle between each group of driving and stowing units remains fixed at 120 degrees. However, as the diameter of the cylindrical structure decreases, the angle between the two layers of axially symmetrical driving and stowing units gradually increases.

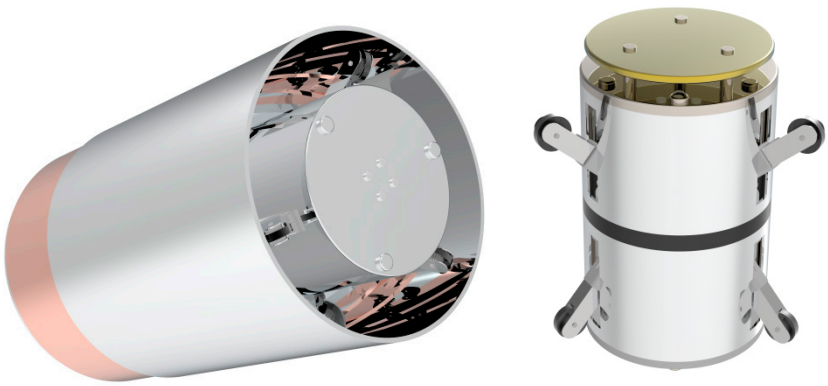

**Figure 16.** The geometric model of the variable-radius inner-drive unit.

We constructed the explicit dynamic coupling field under the radial pre-tensioning load state using the Ansys-Workbench Ls-Dyna module [45]. Figure 17 displays the finite element model of the variable-radius inner-drive unit, comprising 7429 beam elements used to simulate the driving and stowing units experiencing tensile, compressive, and bending loads simultaneously. Additionally, 1847 nonlinear elastic elements are employed to simulate the flexible connection components.

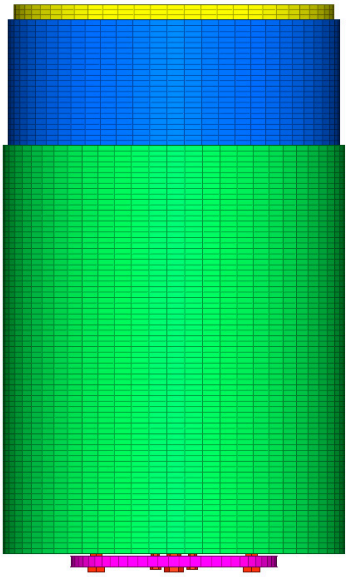

**Figure 17.** The finite element model of the variable-radius inner-drive unit.

To ensure effective analysis and validation, we carefully chose boundary conditions that align with the real operating state of the actual prototype. Additionally, the computational conditions used in the theoretical phase were maintained. The material properties of the driving and stowing units can be found in Table 1.

**Table 1.** Material parameters for the driving-unfolding unit.

| Structural Unit | Material | Elastic Modulus $E$ | Poisson's Ratio $\mu$ | Density $\rho$ |
|---|---|---|---|---|
| Beam structure | Aluminum Alloy (2A14) | 67.7 GPa | 0.33 | 2800 kg/m$^3$ |
| Flexible connectors | Spring Steel (40Cr) | 211 GPa | 0.277 | 7820 kg/m$^3$ |
| Elastomer | JSR | 0.0078 GPa | 0.47 | 1040 kg/m$^3$ |

- Axial forward speed is constant at 5 mm/s;
- Radial pre-tensioning load: 100–150 N. The radial pre-tensioning load is adjusted within this range based on the variation of the cylindrical structure diameter. For instance, the radial pre-tensioning load is higher during the transition between the first-level stages compared to the transition between the second-level stages, and so on;
- Top load: 40 N. The total top load in the full structure state is 120 N, and the designed variable-radius inner-drive unit follows a 120-degree axially symmetrical structure. Therefore, one-third of the structure is used for validating the driving and stowing units;
- Boundary contact: Face-to-face contact is used, and the contact options include sliding friction, rolling friction, and viscoelastic friction in a mixed contact mode. The contact state remains non-offset in the axial direction;
- Deformation setting: Large deformation (flexural deformation) is enabled. The elastic material, JSR, undergoes certain elastic deformation when in contact with the discontinuous rigid surface;
- Ambient temperature: 26 degrees Celsius.

### *3.2. Simulation Analysis*

After partitioning the hexahedral mesh, Parts $L_1$, $L_2$, and $L_3$ are set as beam structures. Figure 18 shows the displacement contour plots of the triangular configuration with thin-walled flexible beam structures under the parallel configuration at time intervals of 0.25 s, 0.5 s, 0.75 s, and 1.0 s. To provide a clearer view of the driving and stowing units, the simulation contour plots only display the driving and stowing units.

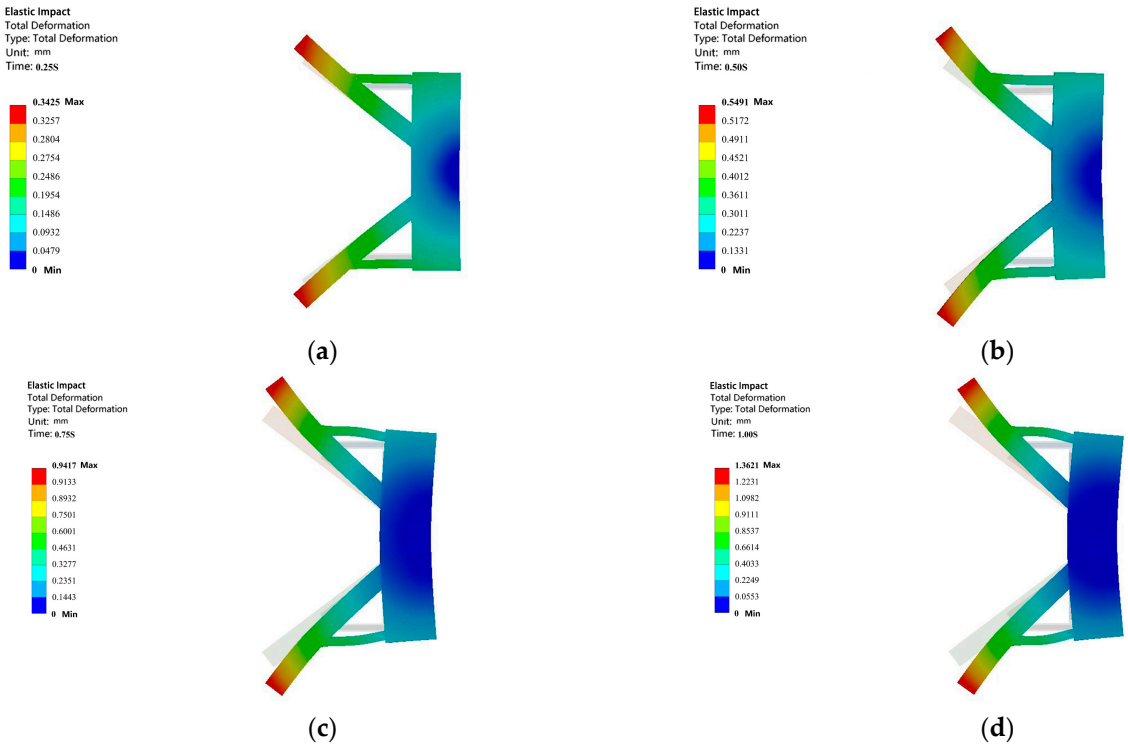


**Figure 18.** The displacement contour plots at different time intervals. (**a**) At the time of 0.25 s; (**b**) At the time of 0.50 s; (**c**) At the time of 0.75 s; (**d**) At the time of 1.00 s.

Figure 18 illustrates the maximum deformations in the x and y directions at different time intervals: 0.25 s, 0.50 s, 0.75 s, and 1.00 s. At 0.25 s, the deformations of points $L_1$, $L_2$, and $L_3$ during the initial stage of the inter-level transition under radial load are not significant, with a maximum deformation of 0.3425 mm. At 0.50 s, points $L_1$ and $L_2$ undergo some bending deformation with a maximum deformation of 0.5491 mm, while point $L_3$ is less affected due to symmetric stress distribution. At 0.75 s and 1.00 s, the maximum deformations in the x and y directions are 0.9417 mm and 1.3621 mm, respectively. During these intervals, point $L_1$ experiences bending deformation only at the front end, point $L_2$ undergoes axial deformation with stress concentrated at the contact area with point $L_1$, and point $L_3$ maintains good bending resistance. Additionally, Figure 19 provides a comparative analysis of the centroid displacements in different directions of the thin-walled flexible beam elements during the theoretical stage depicted in Figure 15.

Figure 19a–c depicts the displacements of the centroid of the drive-unfold unit in the X, Y, and Z directions, respectively. These simulation curves align with the trends observed in the theoretical stage. In the X-direction centroid displacement graph, a series of peaks and valleys appears between 0.2 s and 0.5 s due to radial displacement caused by the transition diameter change during the inter-level transition of the elastic body. The contact between the elastic material and the discontinuous surface rigid body leads to deformation of the elastic material, resulting in a peak-to-peak difference of 1.43 mm in the radial direction. The Y-direction centroid displacement graph shows a phenomenon of axial displacement regression between 0.4 s and 0.6 s, attributed to elastic rebound during the inter-level transition when the elastic body contacts the discontinuous surface rigid body, causing a fluctuation of 0.96 mm. In the Z-direction centroid displacement graph, oscillations occur due to tangential displacement generated by the compression of the elastic body under radial load. During the initial stage of the inter-level transition (between 0.35 s and 0.45 s), the radial load generates stress without adjustment due to the reduction of the transition diameter, leading to increased compression of the elastic body and an associated increase in tangential displacement. However, with timely radial load adjustment, the elastic body undergoes instantaneous radial rebound, resulting in a decrease in tangential displacement.

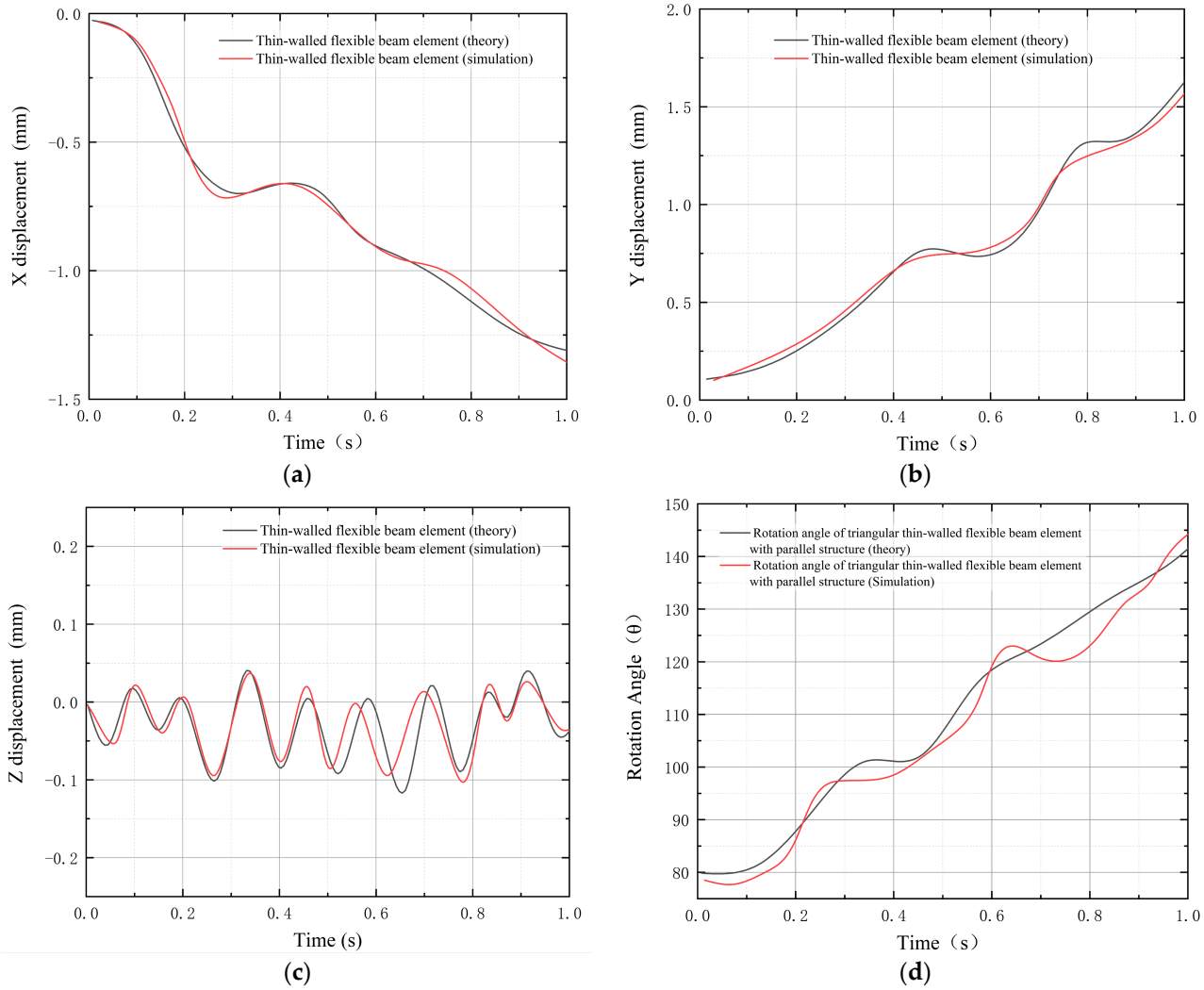


**Figure 19.** The comparison of the displacement trajectories. (**a**) Centroid displacement in the X-direction; (**b**) Centroid displacement in the Y-direction; (**c**) Centroid displacement in the Z-direction; (**d**) Trajectory rotation angle.

Based on the above analysis, the drive-fold unit, when described using the ANCF method for nodal displacements, exhibits consistent mechanical characteristics during the internal motion of the space telescope's tubular deployable structure. Additionally, under the boundary conditions of a moving speed of 5 mm/s and a load of 60 N, the thin-walled flexible beam structure, described by the ANCF method for nodal displacements, demonstrates favorable multidirectional positional variations when subjected to radial preloading and axial frictional forces. This approach brings it closer to the actual state, aiming to improve the motion characteristics of the rigid-flexible coupled deformation and motion precision of the drive-fold unit, ensuring its stability.

## 4. The Experimental Results and Discussion

### *4.1. Inter-Level Transition Test*

To validate the stability of the parallel triangular configuration structure constructed based on the theoretical node displacement description using the absolute nodal coordinate formulation (ANCF), a 1:1 scale experimental prototype was designed and fabricated. The material selection and boundary conditions were set to be consistent with those used in the theoretical and simulation stages. The experimental setup can be referred to in Figure 20.

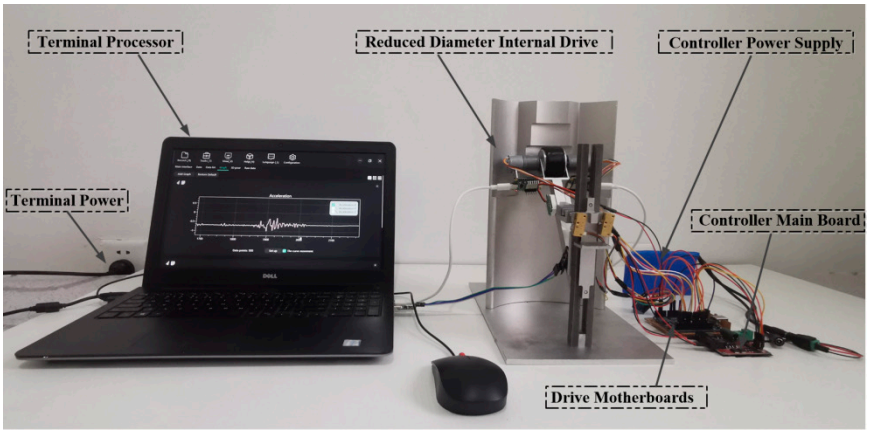


**Figure 20.** Test prototype diagram.

During the experiment, various parameters of the driving and stowing units were monitored using sensors. Figure 21 illustrates the installation positions of the sensors in the experimental prototype. Displacement sensors, velocity sensors, and angle sensors were utilized to measure the endpoint displacement, axial movement velocity, and rotational angle during the unfolding phase of the driving and stowing units.

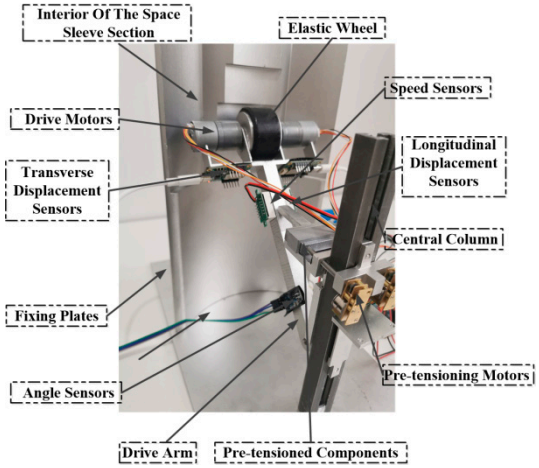


**Figure 21.** Prototype local diagram.

To simplify the motion structure for the experiment, symmetrical elements were chosen within the variable-radius inner-drive unit, as both the driving and stowing units exhibit a symmetrical structure. The experimental setup involved a stepped surface to simulate the non-continuous interior surface of the cylindrical structure. The driving motor was responsible for providing the driving force to an elastic wheel, while the pre-tensioning motor applied a radial pre-tensioning load, pressing the elastic wheel against the stepped surface. Moreover, the driving arm, pre-tensioning components, and pre-tensioning motor were aligned with the central column and equipped with lubricated ball bearings and guide rails. These modifications facilitated axial unfolding, combining the traction force from the elastic wheel with the radial pre-tensioning load from the pre-tensioning components.

The experiment aimed to assess the stability of the parallel triangular configuration structure with thin-walled flexible beam elements after implementing the ANCF method for node displacement description, using the same boundary conditions as in the simulation. Figure 22 illustrates the endpoint displacements in the x and y directions at both the free and constrained ends during the experimental phase. To obtain a more representative result, the data were divided into 40 groups and averaged, resulting in four curves representing the average displacements in the x and y directions for each group.

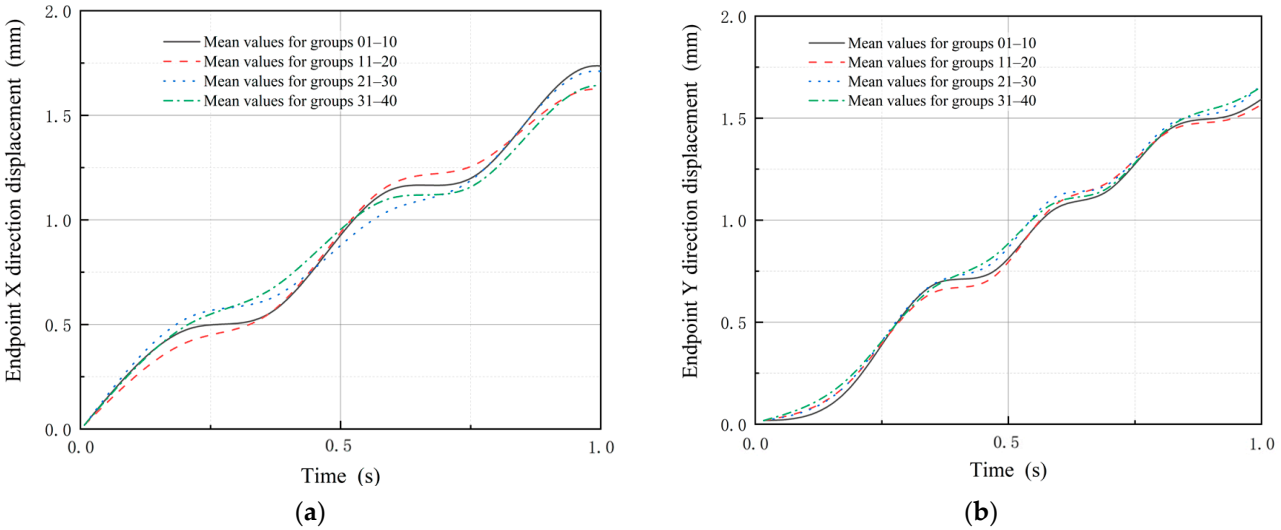


**Figure 22.** The endpoint displacements in the x and y directions. (**a**) The displacement in the X-direction at the endpoints; (**b**) The displacement in the Y-direction at the endpoints.

From Figure 22a,b, we can observe a consistent trend in the average displacements in the x and y directions for the four groups of endpoints during the experimental phase. However, noticeable fluctuations occur at the inter-level discontinuities or steps due to the contact between the stowing unit and the inner wall of the variable-radius inner-drive unit using an elastic wheel. Specifically, at 0.25 s, there is a peak displacement in the x-direction, and between 0.25 s to 0.5 s, there is an axial displacement in the y-direction. This phenomenon is attributed to the transitional phase between levels where the elastic component undergoes deformation, and the driving and stowing unit experiences its first non-continuous surface.

Upon further comparison with the free-end x and y displacements in Figures 10 and 11, it becomes evident that the displacement trends of any group in Figure 22 more accurately reflect the motion state during the same time period. Therefore, combining the free and constrained ends as a complete motion mode for the driving and stowing unit is a valid approach.

Figure 23 illustrates the trajectory angles during the experimental phase. It is observed that the rotational angle exhibits peak changes during the intervals of 0.15–0.25 s, 0.45–0.55 s, and 0.75–0.85 s. This phenomenon is attributed to the transitional phase between levels, involving the rebound effect of the elastic component and the effect of radial pre-tensioning load, which leads to a counterclockwise rotation of the trajectory angle. However, as the driving and stowing unit progresses axially over continuous surfaces and the diameter of the variable-radius inner-drive unit decreases, the trajectory angle undergoes a clockwise rotation, resulting in a further increase in the rotational angle.

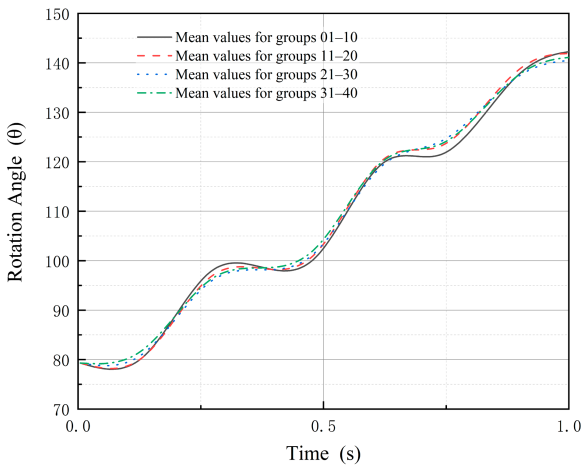


**Figure 23.** Trajectory turning angle.

Figure 23 displays the trajectory angle during the experimental phase. By analyzing the trajectory angle in Figure 23 and comparing it with Figure 19d, we observe that the trajectory angle curves of the four groups in the experimental phase align with the trends observed in the theoretical and simulation phases. Notably, three peaks occur in the same time frame, which can be attributed to the stepped surface. Table 2 presents the displacement and trajectory angle data collected during the combined testing of the prototype at the stepped surface in the three transitional phases.

**Table 2.** Test displacements and angular displacements for the 13 transition stages.

| | Group | | | |
|---|---|---|---|---|
| | **01–10** | **11–20** | **21–30** | **31–40** |
| Transition Order 1—Transverse and Longitudinal Displacement Mean (mm) | 0.48/0.68 | 0.42/0.64 | 0.51/0.68 | 0.49/0.66 |
| Transition Order 2—Transverse and Longitudinal Displacement Mean (mm) | 1.13/1.05 | 1.16/1.07 | 1.04/1.11 | 1.09/1.08 |
| Transition Order 3—Transverse and Longitudinal Displacement Mean (mm) | 1.72/1.45 | 1.62/1.43 | 1.69/1.46 | 1.65/1.45 |
| Transition Order 1—Angular Rotation Mean (θ) | 97.2 | 96.8 | 96.5 | 96.3 |
| Transition Order 2—Angular Rotation Mean (θ) | 119.7 | 120.4 | 119.4 | 120.2 |
| Transition Order 3—Angular Rotation Mean (θ) | 137.9 | 138.2 | 137.5 | 137.8 |

### *4.2. Discussion*

Based on the data obtained from Table 2 during prototype testing at the three transitional phases, we further calculated the average of the four groups to obtain the centroid motion trajectory data of the driving and expanding unit. Subsequently, the trajectory data were fitted, and Figure 24 illustrates the comparison and fitting curves of the driving and expanding unit's trajectories in the theoretical, simulation, and experimental phases.

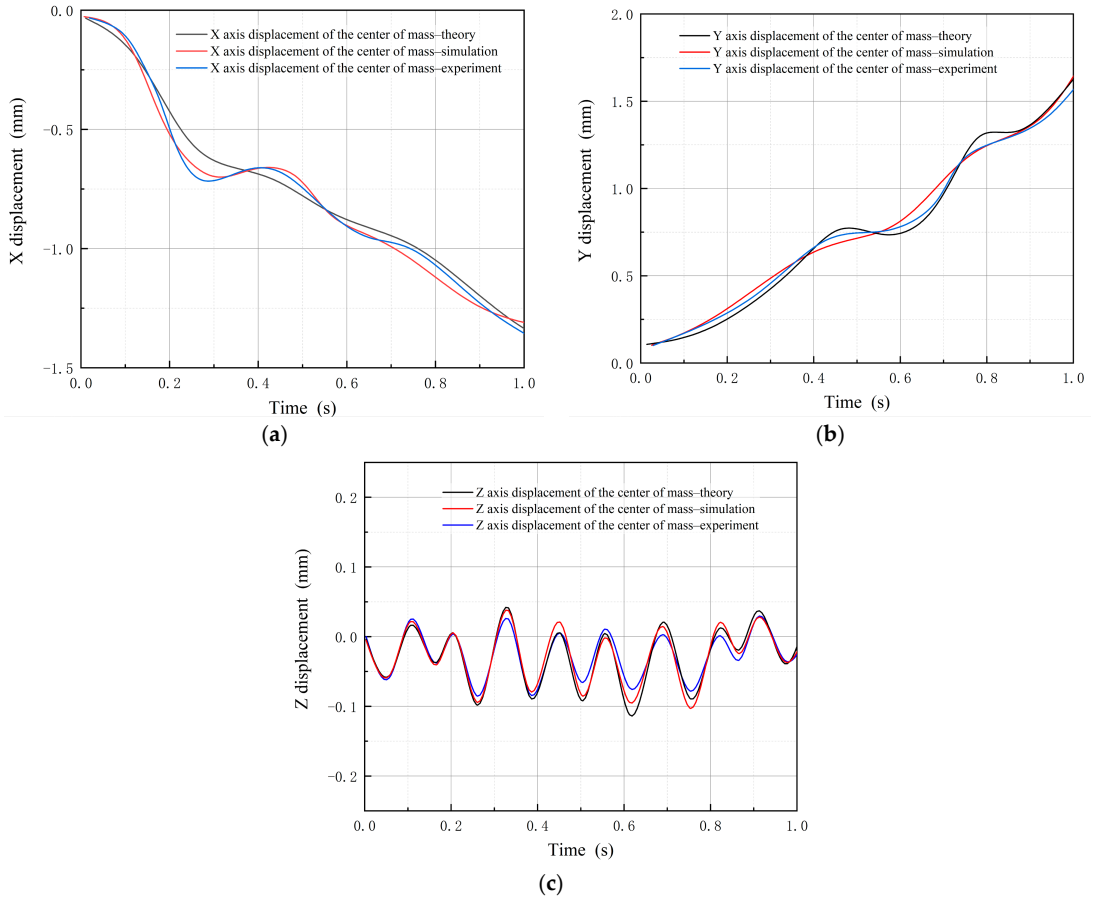


**Figure 24.** Comparison and fitting of trajectories in three stages. (**a**) Displacement in the X-direction of the centroid; (**b**) Displacement in the Y-direction of the centroid; (**c**) Displacement in the Z-direction of the centroid.

Upon analyzing Figure 24a–c, it is evident that the centroid's displacement in three directions of the driving and expanding unit, utilizing thin-walled flexible beam elements described with the absolute nodal coordinate formulation (ANCF), shows a slight reduction in the experimental phase compared to the theoretical and simulation phases. The maximum displacements at peak stages are reduced by 1.81 mm, 2.71 mm, and 0.47 mm, respectively. This reduction is attributed to the friction between the elastic wheel surface and the inner wall of the spatial tube. However, the results indicate that the displacements in all directions are significantly smaller than the dimensional parameters of the driving and expanding unit and the spatial tube structure, demonstrating a high level of stability while effectively accomplishing the climbing motion on the inner wall of the spatial tube.

However, during the experimental phase, the model's beam units were connected using pin connections, which led to some errors attributed to material processing and environmental factors. Nevertheless, these errors were within an acceptable range. Comparing the experimental results with theoretical and simulated data, the maximum error in positional changes during the experimental phase was 0.41%, and the minimum error was 0.32%. These errors occurred during the transition from the first stage to the third stage, likely due to the gradual reduction in the diameter of the spatial sleeve, resulting in more stable mechanical properties. Additionally, Figure 15d indicated that the rotational angle of the parallel triangular configuration of the thin-walled flexible beam unit almost perfectly matched between the simulation and theoretical stages, implying that this error has no significant impact on the trajectory analysis of the driving and retracting unit. Furthermore, considering that the structure operates in a space environment with zero gravity during orbit, such errors can be neglected, especially with the presence of a temperature control system that prevents material properties from affecting the structure.

The experimental results confirmed the excellent stability of the driving and expanding unit with a thin-walled flexible beam structure when operating inside the space telescope's collapsible structure. The experimental findings align closely with the theoretical and simulation analysis results, showing a high level of consistency. The adoption of a thin-walled flexible beam structure in the driving and expanding unit not only enhances the structure's ability to undergo rigid-flexible coupling deformation, improves its dynamic characteristics, and enhances motion precision but also facilitates future lightweight design initiatives. For instance, during the experimental phase, the thin-walled flexible beam structure demonstrated remarkable performance in handling varying loads and maintaining stability. Thus, the use of ANCF theory effectively enables the precise description of node displacements in the triangular configuration of the thin-walled flexible beam structure, ensuring that the constructed driving and expanding unit operates with excellent stability within the space telescope's collapsible structure.

## 5. Conclusions

To align with future space exploration strategies, research has focused on addressing issues related to expansion precision, stiffness, and distance in space telescope collapsible structures when utilizing traditional driving and pre-tensioning devices for axial expansion. In response to the limitations of conventional driving and pre-tensioning devices, the concept of a variable-diameter inner-drive device has been proposed. However, achieving the desired working motion state and design rationality of this variable-diameter inner-drive device necessitates a shift from a conventional flexible beam structure to a thin-walled flexible beam structure. Consequently, there is a need to explore space-based methods for describing the node displacements of the driving and expanding unit with a thin-walled flexible beam structure, aiming to enhance the structure's deformability and improve its motion stability.

This study is based on the theoretical framework of the Space Absolute Nodal Coordinate Formulation (ANCF). Its objective is to analyze the positional states and displacement variations of flexible beam structures, thin-walled flexible beam structures, and parallel structures with triangular configurations at different nodes. To achieve this, the

positional states are transformed into the global coordinate system, obtaining the three-dimensional displacement field and angular rotation variations. The approach involves using global shape functions and unit absolute nodal coordinate vectors to construct the element absolute nodal coordinate vector. Additionally, the element shape function matrix is established by combining the unit shape functions and interpolation polynomials, which is then inserted into the face position vector of the thin-walled flexible beam structure. By taking the derivative with respect to time, the study calculates the element kinetic and strain energies, leading to the derivation of dynamic equations for the thin-walled flexible beam structure. Furthermore, specialized node descriptions are applied for the triangular configurations and parallel structures, and fitting analyses are conducted for the displacement field and attitude of the thin-walled flexible beam structure under both free-end and overall states.

During the validation work, a prototype model of the driving and unfolding unit structure was established. The model incorporated the theoretical node displacement description using the Space absolute nodal coordinate formulation (ANCF) for the thin-walled flexible beam structure. Coupled analyses were conducted to explore the displacement variation cloud maps of the structure at different time intervals in the space environment. The experimental results demonstrated a remarkable consistency between the positional changes at different time intervals and the fitted curves based on the theoretical Space ANCF, with an error range between 0.32% and 0.41%. The correctness of the theoretical Space ANCF in studying the flexible multibody dynamics of the thin-walled flexible beam structure was successfully verified through the design and fabrication of a 1:1 scale experimental prototype. Additionally, the effectiveness of the coupled analysis approach in analyzing the positional responses of the thin-walled flexible beam structure at various time intervals was thoroughly confirmed.

Due to constraints in knowledge and time, this study is considered preliminary compared to the complexity of space exploration structures. As a part of future work, it is essential to investigate the impact of the unit structure itself on elastic friction contact during the inter-level transition phase of the driving deployment unit within the tubular deployable structure of the space telescope. By understanding the friction factors at different times and their relation to the external force applied to the driving deployment unit, the overall stiffness and motion accuracy can be further enhanced.

**Author Contributions:** Conceptualization, W.H. and H.Y.; Methodology, W.H.; Software, Y.G.; Validation, W.H., H.Y. and Y.G.; Formal analysis, H.L., H.W., and W.H.; Investigation, W.H.; Writing—original draft preparation, W.H. and H.Y.; Writing—review and editing, W.H. and H.Y.; Visualization, Y.G.; Supervision, W.H., H.Y. and Y.G.; Project administration, H.L. and H.W.; Funding acquisition, H.Y. All authors have read and agreed to the published version of the manuscript.

**Funding:** This research was funded by National Natural Science Foundation of China, grant number No. 12073028.

**Institutional Review Board Statement:** Not applicable.

**Informed Consent Statement:** Informed consent was obtained from all subjects involved in the study.

**Data Availability Statement:** The data are available from the corresponding author upon reasonable request.

**Acknowledgments:** Many thanks to all the authors who took the time out of their busy schedules to revise and review the paper and provide references.

**Conflicts of Interest:** The authors declare no conflict of interest.

## References

1. Mettler, E.; Breckenridge, W.G.; Quadrelli, M.B. Large Aperture Space Telescopes in Formation: Modeling, Metrology, and Control. *J. Astronaut. Sci.* **2005**, *53*, 391–412. [CrossRef]
2. Lu, S.; Qi, X.; Hu, Y.; Li, B.; Zhang, J. Deployment Dynamics of Large Space Antenna and Supporting Arms. *IEEE Access* **2019**, *7*, 69922–69935. [CrossRef]

3. Liu, G.; Chen, W.; Wang, W.; Chen, Y. Design and analysis of a novel space deployable mechanism of ring and frustum type. *Int. J. Adv. Manuf. Technol.* **2016**, *94*, 3251–3264. [CrossRef]
4. Li, Q.; Liu, L.; Shen, J. One Novel Distributed Space Telescope with Payload Formation. *IEEE Access* **2020**, *8*, 13949–13957. [CrossRef]
5. Sun, Z.; Yang, D.; Duan, B.; Kong, L.; Zhang, Y. Structural design, dynamic analysis, and verification test of a novel double-ring deployable truss for mesh antennas. *Mech. Mach. Theory* **2021**, *165*, 104416. [CrossRef]
6. Cheng, P.; Ding, H.; Cao, W.-A.; Gosselin, C.; Geng, M. A novel family of umbrella-shaped deployable mechanisms constructed by multi-layer and multi-loop spatial linkage units. *Mech. Mach. Theory* **2020**, *161*, 104169. [CrossRef]
7. Zhao, N.; Luo, Y.; Wang, G.; Shen, Y. A deployable articulated mechanism enabled in-flight morphing aerial gripper. *Mech. Mach. Theory* **2021**, *167*, 104518. [CrossRef]
8. Liu, S.; Li, Q.; Wang, P.; Guo, F. Kinematic and static analysis of a novel tensegrity robot. *Mech. Mach. Theory* **2020**, *149*, 103788. [CrossRef]
9. Yang, Y.; Liu, H.; Zheng, H.; Peng, Y.; Yu, Y. Two types of remote-center-of-motion deployable manipulators with dual scissor-like mechanisms. *Mech. Mach. Theory* **2021**, *160*, 104274. [CrossRef]
10. Zhong, B. The Design and Analysis of Telescope Mast. Doctoral Dissertation, Harbin Instituteof Technology, Harbin, China, 2008.
11. Mobrem, M.; Spier, C. Design and Performance of the Telescopic Tubular Mast. In Proceedings of the 41st Aerospace Mechanisms Symposium, Pasadena, CA, USA, 16–18 May 2012; pp. 1–14.
12. Guan, F.; Cao, N. Research on a Space Expandable Telescopic Mechanism. *J. Vib. Shock.* **2019**, *38*, 103–109.
13. Sofla, M.S.; Sadigh, M.J.; Zareinejad, M. Design and dynamic modeling of a continuum and compliant manipulator with large workspace. *Mech. Mach. Theory* **2021**, *164*, 104413. [CrossRef]
14. Zhang, Z.; Tang, S.; Fan, W.; Xun, Y.; Wang, H.; Chen, G. Design and analysis of hybrid-driven origami continuum robots with extensible and stiffness-tunable sections. *Mech. Mach. Theory* **2021**, *169*, 104607. [CrossRef]
15. Malm, C.G.; Davids, W.G.; Peterson, M.L.; Turner, A.W. Experimental characterization and finite element analysis of inflated fabric beams. *Constr. Build. Mater.* **2009**, *23*, 2027–2034. [CrossRef]
16. Zuqing, Y. New Element Construction of Absolute Node Coordinate Method and Its Application in Vehicle System Dynamics. Master Dissertation, Harbin Instituteof Technology, Harbin, China, 2016.
17. Jingchen, H. WANG Tianshu. Research on a recursive absolute node coordinate method with O (n) algorithm complexity. *J. Mechanics.* **2016**, *48*, 1172–1183.
18. Shabana, A.A. Flexible Multibody Dynamics: Review of Past and Recent Developments. *Multibody Syst. Dyn.* **1997**, *1*, 189–222. [CrossRef]
19. Shabana, A.A. *Dynamics of Multibody Systems*; Cambridge University Press: Cambridge, UK, 2013.
20. Shabana, A.A. *An Absolute Nodal Coordinate Formulation for the Large Rotation and Deformation Analysis of Flexible Bodies*; Technical Report; Department of Mechanical Engineering, University of Illinois at Chicago: Chicago, IL, USA, 1996.
21. Shabana, A.A. *Computational Continuum Mechanics*; John Wiley & Sons: Hoboken, NJ, USA, 2018.
22. Zhang, D. Research on modeling and numerical solution algorithm of flexible beam based on absolute node coordinate method. Doctoral Dissertation, Northwestern Polytechnical University, Xi'an, China, 2019.
23. Li, B. New Thin-Walled Beam Element Based on Absolute Node Coordinate Method. Doctoral Dissertation, Yanshan University, Qinhuangdao, China, 2020.
24. Shiyang, L. Dynamic Modeling and Motion Control of Spacecraft Flexible Attachments Based on Absolute Node Coordinates. Doctoral Dissertation, Harbin Instituteof Technology, Harbin, China, 2021.
25. Wu, M.; Tan, S.; Gao, F. Deformation reconstruction of plane beam under finite deformation based on absolute node coordinate method. *J. Mech.* **2021**, *53*, 2776–2789.
26. Luo, K.; Liu, C.; Tian, Q.; Hu, H. Nonlinear static and dynamic analysis of hyper-elastic thin shells via the absolute nodal coordinate formulation. *Nonlinear Dyn.* **2016**, *85*, 949–971. [CrossRef]
27. Li, Q.; Deng, Z.; Zhang, K.; Huang, H. Unified Modeling Method for Large Space Structures Using Absolute Nodal Coordinate. *AIAA J.* **2018**, *56*, 4146–4157. [CrossRef]
28. Zhang, C.; Kang, Z.; Ma, G.; Xu, X. Mechanical modeling of deepwater flexible structures with large deformation based on absolute nodal coordinate formulation. *J. Mar. Sci. Technol.* **2019**, *24*, 1241–1255. [CrossRef]
29. Pechstein, A.; Gerstmayr, J. A Lagrange–Eulerian formulation of an axially moving beam based on the absolute nodal coordinate formulation. *Multibody Syst. Dyn.* **2013**, *30*, 343–358. [CrossRef]
30. Wang, G. Elastodynamics modeling of 4-SPS/CU parallel mechanism with flexible moving platform based on absolute nodal coordinate formulation. *Proc. Inst. Mech. Eng. Part C J. Mech. Eng. Sci.* **2017**, *232*, 3843–3858. [CrossRef]
31. Hu, J.; Wang, T. An o(n) complexity recursive algorithm for multi-flexible-body dynamics based on absolute nodal coordinate formulation. *Int. J. Numer. Methods Eng.* **2016**, *110*, 1049–1068. [CrossRef]
32. Yang, D.; Yu, H.; Lin, Z. Dynamic Analysis and Optimal Parameter Design of Flexible Composite Structures via Absolute Nodal Coordinate Formulation. *J. Shanghai Jiaotong Univ. (Sci.)* **2022**, *30*, 1–9. [CrossRef]
33. Sheng, F.; Zhong, Z.; Wang, K.-H. Theory and model implementation for analyzing line structures subject to dynamic motions of large deformation and elongation using the absolute nodal coordinate formulation (ANCF) approach. *Nonlinear Dyn.* **2020**, *101*, 333–359. [CrossRef]

34. Wang, D. Solar Sail Trajectory Design and Optimization Based on Shape Function Method. Doctoral Dissertation, Harbin Institute of Technology, Harbin, China, 2002.
35. Iwai, R.; Kobayashi, N. A New Flexible Multibody Beam Element Based on the Absolute Nodal Coordinate Formulation Using the Global Shape Function and the Analytical Mode Shape Function. *Nonlinear Dyn.* **2003**, *34*, 207–232. [CrossRef]
36. Song, S.; Liu, Z. A second-order isoparametric element method to solve plane linear elastic problem. *Numer. Methods Partial. Differ. Equations* **2020**, *37*, 1535–1550. [CrossRef]
37. Rathod, H. Some analytical integration formulae for a four node isoparametric element. *Comput. Struct.* **1988**, *30*, 1101–1109. [CrossRef]
38. Zhou, J. Research on Dynamic Characteristics of a Class of Slender Truss Spacecraft. Master Dissertation, Harbin Instituteof Technology, Harbin, China, 2017.
39. Feng, X.; Liang, L.; Song, H. Application of Lagrange's equation to rigid-elastic coupling dynamics. *Sci. China Technol. Sci.* **2017**, *1*, 247–1277. [CrossRef]
40. Acharyya, S.; Mandal, M. Performance of EAs for four-bar linkage synthesis. *Mech. Mach. Theory* **2009**, *44*, 1784–1794. [CrossRef]
41. Delphenich, D.H. A generalized Hamiltonian formulation of the principle of virtual work. *Math. Phys.* **2022**, *23*, 25–33.
42. Xiao, S. Dynamics Analysis and Optimization of Spatial Parallel Mechanisms. Master Dissertation, Changzhou University, Changzhou, China, 2021.
43. Lee, D.I.; Kwak, B.M. A direct integration method of elastodynamics using finite element time discretization. *Comput. Struct.* **1993**, *47*, 201–211. [CrossRef]
44. Szafran, J.; Juszczyk, K.; Kamiński, M. Experiment-based reliability analysis of structural joints in a steel lattice tower. *J. Constr. Steel Res.* **2019**, *154*, 278–292. [CrossRef]
45. Rust, W.; Schweizerhof, K. Finite element limit load analysis of thin-walled structures by ANSYS (implicit), LS-DYNA (explicit) and in combination. *Thin-Walled Struct.* **2003**, *41*, 227–244. [CrossRef]